




RESEARCH ARTICLE | MARCH 05 2024

MHD stability of spherical tokamak equilibria with non-monotonic q-profiles ^{EP}

S. C. Jardin ; S. Munaretto ; N. M. Ferraro ; S. M. Kaye ; A. Kleiner ; B. C. Lyons 

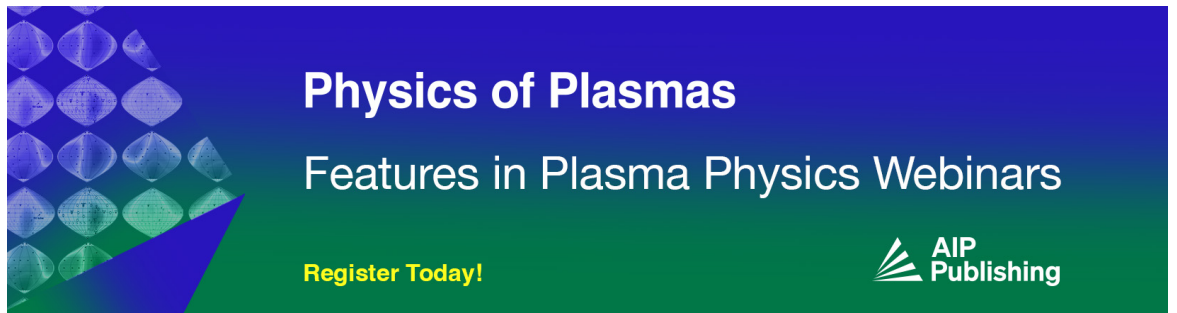


Phys. Plasmas 31, 032503 (2024)

<https://doi.org/10.1063/5.0191934>




CrossMark



Physics of Plasmas
Features in Plasma Physics Webinars

Register Today!



MHD stability of spherical tokamak equilibria with non-monotonic q-profiles

Cite as: Phys. Plasmas **31**, 032503 (2024); doi: [10.1063/5.0191934](https://doi.org/10.1063/5.0191934)

Submitted: 17 December 2023 · Accepted: 11 February 2024 ·

Published Online: 5 March 2024



View Online



Export Citation



CrossMark

S. C. Jardin,^{1,a)}  S. Munaretto,¹  N. M. Ferraro,¹  S. M. Kaye,¹  A. Kleiner,¹  and B. C. Lyons² 

AFFILIATIONS

¹Princeton Plasma Physics Laboratory, P.O. Box 451, Princeton, New Jersey 08543, USA

²General Atomics, P.O. Box 85608, San Diego, California 92186, USA

^{a)}Author to whom correspondence should be addressed: jardin@pppl.gov

ABSTRACT

We use the 3D magnetohydrodynamic (MHD) code M3D-C¹ [Jardin *et al.*, *Comput. Sci. Discovery* **5**, 014002 (2012)] to examine the MHD stability and subsequent evolution of NSTX shot 129169. This discharge had a period with a non-monotonic safety factor profile, q (reversed shear), which was terminated by a MHD event that abruptly lowered the central safety factor, q_0 , and greatly reduced the peakedness of the pressure profile. We show that the equilibrium just before the MHD event occurred was linearly unstable to many pressure-driven infernal modes. Modes with toroidal mode number $n \geq 3$ all had rational surfaces very close to the minimum value of q . However, a non-resonant pressure-driven (1, 1) mode was also present, and this dominated the nonlinear evolution. The final state in the simulation, after the MHD activity subsided, had a reduced and flattened pressure profile and a nearly monotonic q -profile, in qualitative agreement with experimental results. The initial state was also unstable to the resistive interchange criteria in the reversed-shear region, but the final state was stable everywhere. The “double tearing mode” (DTM) does not appear to play a role in the MHD activity of this discharge. In Appendix A, we show that in a torus, the DTM is strongly stabilized by pressure, but it is destabilized in cylindrical geometry (which has been the most extensively analyzed in the literature).

Published under an exclusive license by AIP Publishing. <https://doi.org/10.1063/5.0191934>

I. INTRODUCTION

Recent and present-day spherical tokamaks such as NSTX,¹ MAST,² NSTX-U,³ MAST-U,⁴ and Globus-M⁵ tend to have relatively short pulses, where external heating power is applied before the current profile is fully penetrated and relatively stationary. This makes them potentially susceptible to a class of pressure-driven magnetohydrodynamic (MHD) instabilities that can occur when the central safety factor is above unity, $q_0 > 1$.

Several recent papers have examined the MHD stability of NSTX discharges with monotonic q -profiles in which neutral-beam heating power was applied early in the discharge when the central safety factor was well above unity.^{6–8} It was found that both non-resonant and resonant (infernal mode) MHD instabilities could be excited, in some cases destroying the innermost flux surfaces, leading to a flattening of the electron temperature profile.

Here, we extend this analysis to examine early-time NSTX discharges in which the q -profile is non-monotonic (i.e., reversed shear). These can arise when early central heating is applied and often are associated with a “transport barrier” leading to elevated electron and

ion temperatures. However, these discharges are often accompanied by a “MHD event,” which affects the improved confinement.^{9,11}

Several authors have used 3D MHD codes to study the MHD stability properties of reversed-shear discharges in conventional aspect ratio tokamaks, including DIII-D,¹² TFTR,^{13–15} Tore-Supra,^{16,17} JET,^{18,19} JT-60SA,²⁰ and some generic configurations.^{21,22} These and other calculations have highlighted the role of resistive interchange modes,¹² the (2,1) double tearing mode (DTM),^{15,23,24} the (3,1) DTM,^{25,26} and ballooning, infernal, and resonant modes.²⁰ These unstable modes can lead to localized pressure crashes,^{15,24} explosive bursts,^{21–23,26} reconnection,^{19,25} and/or confinement degradation.^{18,20}

In Sec. II, we summarize the experimentally observed MHD properties of NSTX reversed-shear discharge 129169. In Sec. III, we examine the linear stability properties of this discharge at a time just before a MHD event was observed to occur in the experimental discharge. Section IV presents the results of a 3D nonlinear MHD simulation starting from this time in which both a minor and a semi-major MHD event occur (*not* a DTM). The first MHD event affects the pressure profile, and the second alters both the current and pressure

profiles sufficiently so that the discharge becomes completely MHD stable and the flux surfaces re-form. This stable final state is discussed in Sec. V. In Sec. VI, we provide a summary with some discussion. We also include Appendix A in which we discuss the stability to DTMs of a model equilibrium with reversed shear in both cylindrical and toroidal geometry. It is shown that pressure is strongly stabilizing to DTMs in toroidal geometry, while it is strongly destabilizing in cylindrical geometry.

II. A TYPICAL CASE

Consider NSTX shot 129169, which had central reversed shear early in the discharge and was of interest because of the transport barriers associated with the reversed-shear region.⁹ The reconstructed safety factor and surface averaged pressure profiles for several times are shown in Fig. 1, and magnetic fluctuation data are shown in Fig. 2. The equilibria were reconstructed with the LRDFIT code¹⁰ using magnetics, motional Stark effect (MSE), temperature isotherms, and rotation constraints.

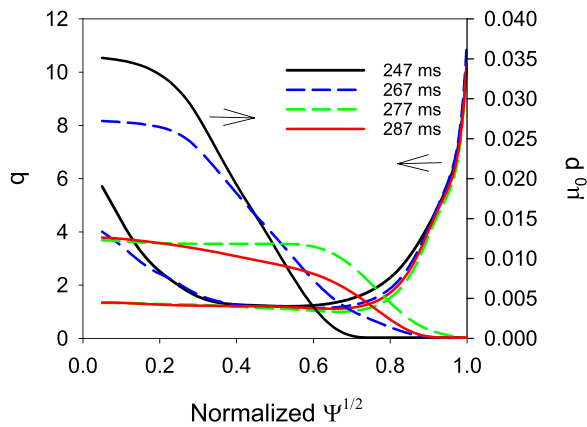


FIG. 1. Experimentally reconstructed profiles for the safety factor and surface averaged pressure from NSTX shot 129169 at four times.

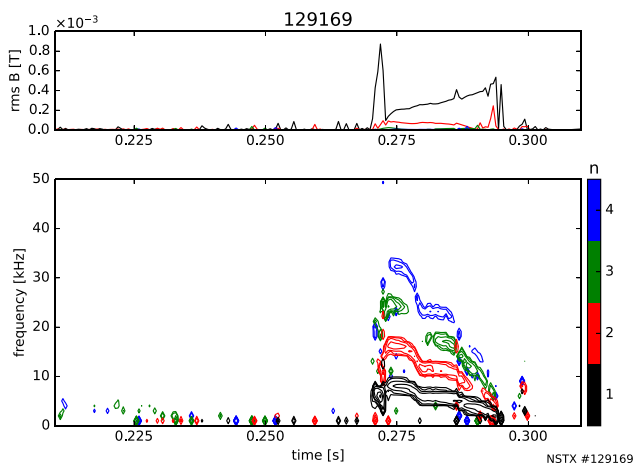


FIG. 2. Magnitude and frequencies of MHD activity during the period 215–310 ms.

This discharge had a toroidal field of 0.55 T and a flattop current of 1 MA. It was an L-mode discharge, heated by neutral beam injection (NBI) and high harmonic fast wave (HHFW). We examine the linear and nonlinear stability properties of this discharge at time $t = 247$ ms in Secs. III and IV. The central electron temperature was about 2.8 keV at this time.

It is clear from Fig. 2 that some MHD activity began just before 270 ms. From the top graph in Fig. 2, it is seen that there was first a strong rapid onset toroidal mode number $n = 1$ signal, starting at about 270 ms and lasting only a ms or less. This is followed by a more slowly growing $n = 1$ mode that grows for about 20 ms and then disappears. From Fig. 1, it is seen that both the pressure and q -profiles changed significantly during this period between 267 and 277 ms, presumably due to the MHD activity.

Also seen from Fig. 1 is that there is a broadening of the pressure profile that occurs between 247 and 267 ms. Figure 2 does not show any obvious MHD activity during this time, but it could be associated with a purely internal MHD mode that did not register a signal on the external δB probe.

III. LINEAR STABILITY PROPERTIES

In this section, we first present the results of a linear stability analysis of the equilibrium of interest using the linearized version of the M3D-C¹ code. The equations being solved are the linearized form of those given in Sec. V. We also compute the linear stability of the same configuration but with the resistivity and pressure varied to better understand the nature of the unstable modes. We also evaluate the equilibrium with regard to a local criteria for resistive interchange modes.

The equilibrium at time $t = 247$ ms is unstable to many MHD modes, the eigenfunctions of the first 8 are shown in Fig. 3. We show in Fig. 4 the computed growth rates of the first 18 unstable modes ($n = 1 - 18$) using the actual Spitzer resistivity. Also shown in the figure (dashed lines) are the growth rates when the resistivity is increased everywhere by a factor of 10. The fact that these differ by only a few percent for modes with $n > 2$ indicates that these are ideal MHD modes.

As a further check on this, we repeated the stability calculations with zero resistivity. The growth rates were reduced by less than 1%, except for the $n = 2$ mode, for which we could not get a convergent result at zero resistivity.

To better understand the drive for these instabilities, we generated a series of equilibrium with the same q -profile but reduced pressure profiles. Also shown in Fig. 4 are the stability results for an equilibrium so generated with β reduced by 5%, but the central value of pressure is reduced by 12% (slightly broadened pressure profile). The fact that the growth rates are greatly reduced (or made stable) indicates that these are pressure-driven modes.

For each n , the eigenfunction develops a distinct poloidal mode number m , as shown in Fig. 3. These are listed in Table I. We see that the ratio of m/n in the table for $n > 2$ ranges from 1.20 to 1.33. The minimum value of q in this equilibrium is 1.203, so these modes mostly have resonances where $m - nq = 0$ very close to the minimum value of q , though several are slightly non-resonant (with $m/n < 1.203$). These are infernal modes, similar to those found in studies with monotonic q -profiles.^{6,7,27}

The $n = 1$ linear instability is predominantly a non-resonant $m = 1$ mode. It is somewhat less localized to a particular surface than

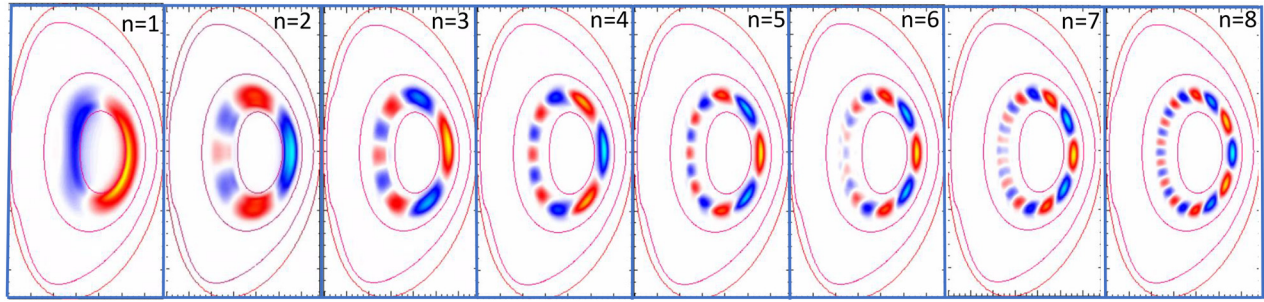


FIG. 3. The first eight linear eigenfunctions showing the perturbed pressure for the reconstructed equilibrium from NSTX shot 129169 at 247 ms. Also shown in each frame are the $2q=2$ contours, the plasma/vacuum boundary, and the computational boundary.

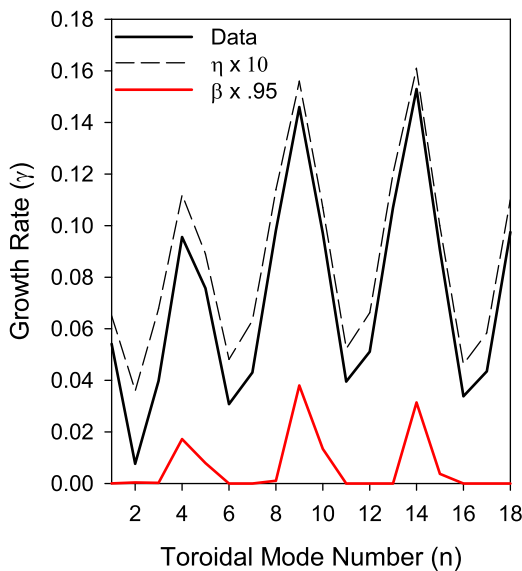


FIG. 4. Growth rates for the first 18 linearly unstable modes for the reconstructed equilibrium from NSTX shot 129169 at 247 ms using Spitzer resistivity (black solid) and ten times Spitzer resistivity (black dashed). Also shown are the growth rates when the β is reduced by 5% (peak central pressure by 12%).

TABLE I. Poloidal mode number m for each of first 18 unstable modes shown in Fig. 4.

n	1	2	3	4	5	6	7	8	9	10	11	12	13	14	15	16	17	18
m	1	3	4	5	6	7	9	10	11	12	13	15	16	17	18	20	21	22

the higher- n modes. It is also predominately an *ideal MHD* mode as its growth rate changes very little as the resistivity is increased by a factor of 10.

It has been known since the 1960s that confinement configurations that are stabilized against ideal interchange instabilities²⁸ primarily by magnetic shear can be subject to resistive interchange instabilities in the presence of resistivity.²⁹ In the 1970s, a general local criterion for stability to resistive interchange instabilities was

derived.^{30,31} It was shown that if the surface quantity, D_R (see Appendix C), was positive, a resistive interchange instability could occur with a growth rate proportional to the $1/3$ rd power of the resistivity. Several authors have noted that reversed shear discharges with peaked pressures can be unstable to resistive interchange modes.^{10,12,32,33}

The equilibrium reconstructed at time $t = 247$ ms had D_R positive in the region interior to the minimum value of q , indicating instability to the resistive interchange mode in this region. We return to this in Sec. V. However, this is apparently not the dominant instability for all n except possibly $n = 2$, which has a relatively small growth rate that does increase when the resistivity is increased.

As noted earlier, these modes are all *pressure driven*. It is likely that the actual experimental profiles were at or near marginal stability at the time of this equilibrium reconstruction as the error in the equilibrium reconstruction has not been taken into account. Also, kinetic effects and sheared rotation, not included in our calculation, could be stabilizing these modes near the marginal point.

We note here that although there are many unstable modes, they are all localized near the same rational surface. We call them different modes because they have different n and m values, but they largely overlap in the poloidal flux coordinate.

IV. A NONLINEAR SIMULATION

We show in Figs. 5–9, the results of a 3D nonlinear simulation, starting from the equilibrium considered in Sec. III. (To clarify the essential 3D effects, we also have performed a 2D axisymmetric calculation using the same transport coefficients.) For these calculations, we used the single fluid option of the nonlinear M3D-C¹ code³⁴ in which the following equations are evolved in time:

$$\frac{\partial n}{\partial t} + \nabla \cdot (n\mathbf{V}) = \nabla \cdot D\nabla n, \quad (1)$$

$$\frac{\partial \mathbf{A}}{\partial t} = -\mathbf{E} - \nabla\Phi, \quad (2)$$

$$\nabla_{\perp} \cdot \frac{1}{R^2} \nabla\Phi = -\nabla_{\perp} \cdot \frac{1}{R^2} \cdot \mathbf{E}, \quad (3)$$

$$\mathbf{E} + \mathbf{V} \times \mathbf{B} = \eta \mathbf{J} - \lambda_H \Delta^* J_{\phi} \nabla\phi, \quad (4)$$

$$nM_i \left(\frac{\partial \mathbf{V}}{\partial t} + \mathbf{V} \cdot \nabla \mathbf{V} \right) + \nabla p = \mathbf{J} \times \mathbf{B} - \nabla \cdot \Pi, \quad (5)$$

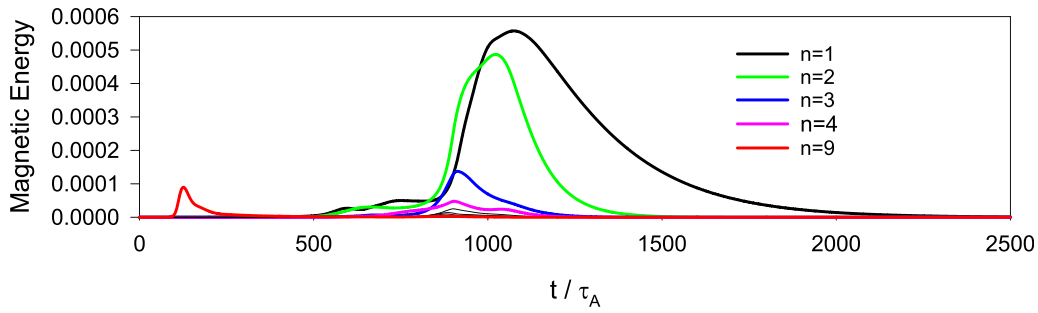


FIG. 5. The magnetic energy in the different toroidal harmonics vs time for the nonlinear M3D-C¹ simulation. Energies for $n = 5 - 8$ and $n \geq 9$ are included in the calculation but are negligible for all times plotted. Note: $1 \tau_A = 0.00046$ ms.

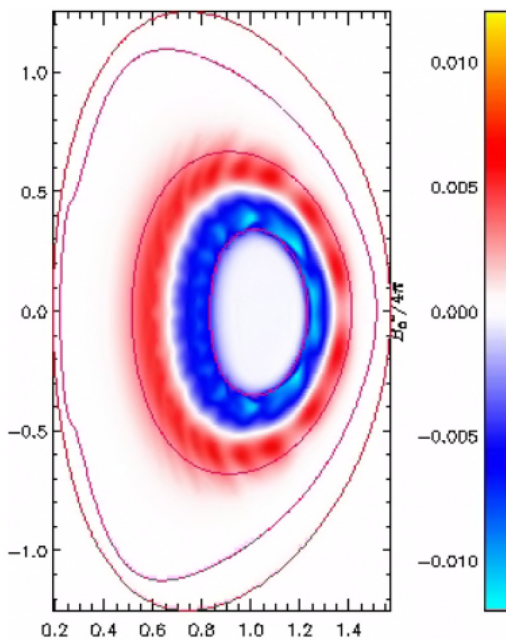


FIG. 6. Contours of the *difference* in the pressure at time $300 \tau_A$ from that at time 0 in the simulation. Also shown are the two contours of the $q=2$ surfaces, the LCFS, and the computational boundary. (2D contour plot is at the $\phi = 0$ plane.)

$$\frac{3}{2} \left[\frac{\partial p}{\partial t} + \nabla \cdot (p\mathbf{V}) \right] = -p\nabla \cdot \mathbf{V} + \mathbf{J} \cdot \mathbf{E} - \nabla \cdot \mathbf{q} + S_E. \quad (6)$$

The magnetic field and current density are then determined by $\mathbf{B} = \nabla \times \mathbf{A}$ and $\mathbf{J} = \nabla \times \mathbf{B}$, respectively. The symbol ∇_{\perp} in Eq. (3) refers to the gradient in the (R, Z) plane in a (R, ϕ, Z) cylindrical coordinate system, and Δ^* is the standard toroidal elliptic operator that appears in the Grad-Shafranov equation. Equation (3) follows from the gauge condition on \mathbf{A} , $\nabla_{\perp} \cdot R^{-2}\mathbf{A} = 0$. The temperature is the pressure divided by the density, $T \sim p/n$. The linear form of the code used for linear stability studies is just the linearized form of these same equations.

The particle diffusion term D in Eq. (1) is a small term included to aid numerical stability. The resistivity η in Eq. (4) is the

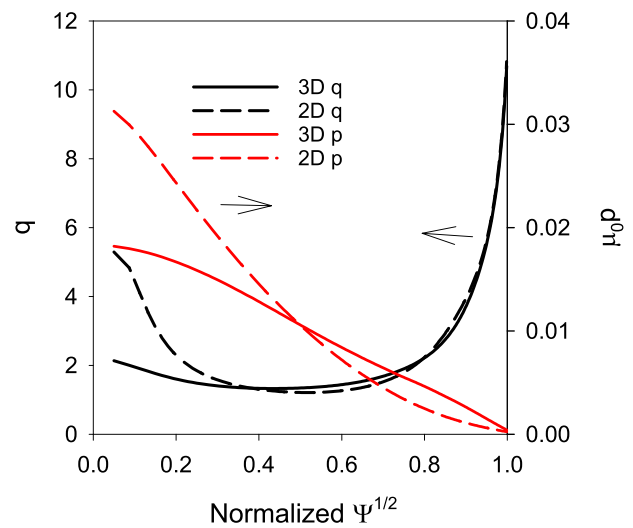


FIG. 7. Shown in solid are the q -profile and surface averaged pressure profile at the end of the nonlinear calculation. Also shown, in dashed lines, are the q and p profiles for a companion 2D calculation with the same transport coefficients.

temperature-dependent Spitzer function³⁵ with possible enhancement as described in Appendix B. The term involving λ_H is hyper-resistivity. A small value is used to improve numerical stability as discussed in Appendix B.

The stress tensor in Eq. (5) is of standard form for viscosity,³⁶ with viscosity coefficient μ . The heat flux vector, \mathbf{q} , in Eq. (6) has both an isotropic part and a part parallel to the magnetic field: $\mathbf{q} = -\kappa \nabla T - \kappa_{\parallel} \mathbf{b} \mathbf{b} \cdot \nabla T$, where \mathbf{b} is a unit vector in the direction of the magnetic field. The numerical values of the transport coefficients used in the calculation are given in Appendix B.

Note that the source term S_E given in Eq. (6) was zero for these calculations. An energy source is not needed to sustain the profiles for a calculation spanning such short times with such small transport coefficients.

The M3D-C¹ code uses finite elements in all three dimensions. In the (R, Z) plane, these are unstructured “Bell” triangular elements³⁷ that, for the baseline calculation, have a typical size of 1.2 cm, with a total of 26 130 vertices per plane. In these calculations, we used 24 planes, with structured equally spaced Hermite cubic finite elements.

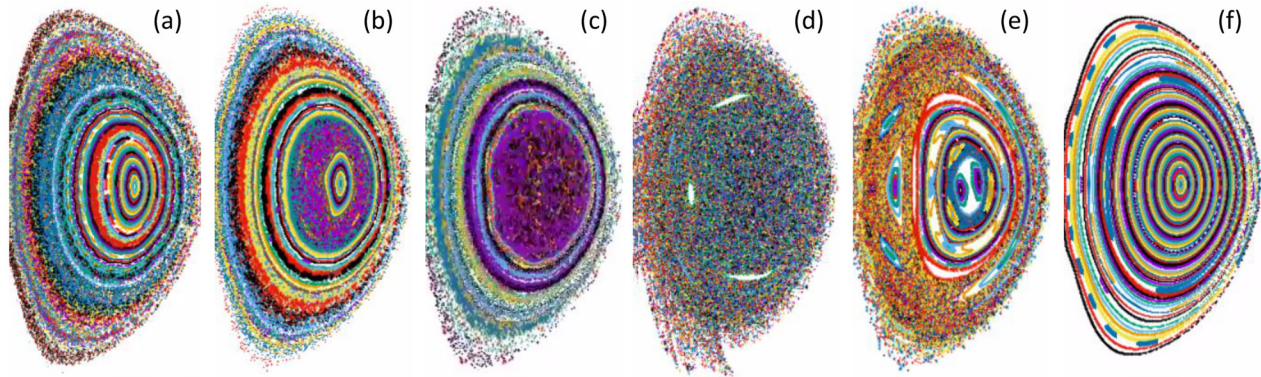


FIG. 8. Poincaré plots at times (a) $300 \tau_A$, (b) $500 \tau_A$, (c) $700 \tau_A$, (d) $900 \tau_A$, (e) $1400 \tau_A$, and (f) $2500 \tau_A$.

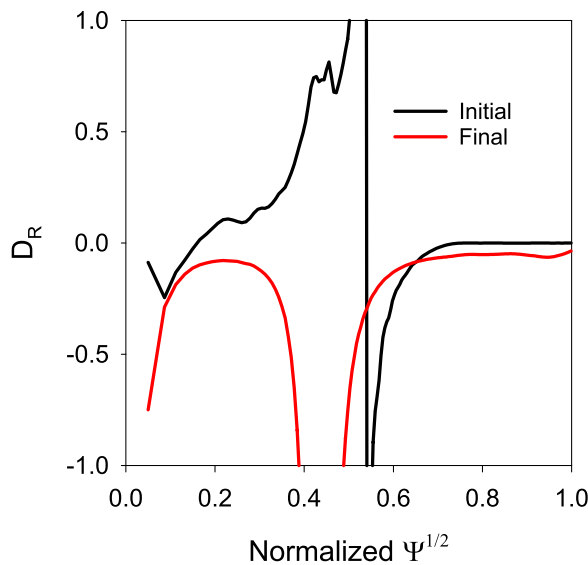


FIG. 9. The resistive interchange (RI) stability parameter, D_R ,³¹ as a function of the square root of the normalized poloidal flux for the nonlinear calculation described in Sec. IV and depicted in Figs. 5 and 8. Plasma is unstable to RI if $D_R > 0$.

As seen in Fig. 6, the computational grid extends slightly beyond the last closed flux surface (LCFS). The region between the LCFS and the computational boundary is treated as a high-resistivity low pressure plasma.

In Fig. 5, we plot the magnetic energy in the dominant toroidal harmonics as a function of time for the 3D nonlinear calculation. It is seen from the figure that there are two seemingly disconnected events occurring in the time interval 0–2500 τ_A (about 1.0 ms) after the start at time 247 ms. The first event, peaking at about 125 τ_A , involves primarily a $n = 9$ mode, which, we see from Fig. 4, had one of the highest linear growth rates. The second, higher amplitude and longer lasting event peaks at about 1100 τ_A . It predominantly involves modes with $n = 1, 2, 3$, and 4.

To see the effect of the first event, we show in Fig. 6 contours of the difference in the pressure at time 300 τ_A from that at time 0 in the

simulation. Also shown are the two contours of the $q = 2$ surfaces, the LCFS, and the computational boundary. It is seen that the effect of the first instability event was to slightly redistribute the pressure in the region interior to the $2 q = 2$ surfaces.

We plot in Fig. 7 the q and pressure profiles at the end of the 3D nonlinear calculation. Also shown are the same profiles at the end of the companion 2D (axisymmetric) calculation with the same transport coefficients. We see that the effect of the 3D instabilities was to lower both the central safety factor and the central pressure.

We note here the central role of the $n = 1$ mode in modifying the central p and q profiles. This is an ideal, non-resonant, pressure-driven mode. It is the only mode with a substantial $m = 1$ component, which is needed to affect the profiles near the magnetic axis.

The 3D MHD calculation presented here was performed on the Perlmutter supercomputer at NERSC. It utilized 1152 processors and required a wall-clock time of over 200 h.

V. A FINAL STABLE STATE

The final state of the 3D nonlinear MHD calculation presented in Sec. IV is nearly axisymmetric and apparently completely MHD stable. A blow-up of the magnetic energy vs time plot of Fig. 5 shows that the energy in all the diagnosed toroidal harmonics, up to $n = 12$, has magnitudes that are decreasing in time at $t = 2500 \tau_A$. Figure 8(f) shows that the surfaces have largely reformed with only a few small island chains, most notably a $(3, 1)$ island near the $q = 3$ surface.

We see from Fig. 7 that the central safety factor, q_0 , has dropped from near 6 to just above 2, greatly reducing the region of reversed shear and its magnitude. In Fig. 9, we plot the resistive interchange stability parameter D_R at the initial and final time of the nonlinear calculation. We see that at the final time, it is negative everywhere, indicating stability to resistive interchange modes. This is due to both the reduction in the magnitude of the reversed shear region and the reduction of the pressure gradient in this region as seen in Fig. 7.

In this calculation, the plasma β was reduced from 3% to 2.3%, while the central pressure declined from $\mu_0 p = 0.035$ to $\mu_0 p = 0.018$. To better understand if it was the drop in q_0 or the decrease in the pressure that most influenced the stability to the resistive interchange modes, we produced another equilibrium with the same q -profile as in the initial state but with a reduced pressure with a $\beta = 1.9\%$ and a central value of $\mu_0 p = 0.020$. This equilibrium still had a positive D_R

in the reversed-shear region, although at lower values than the original. This indicates that the reversed shear is critical for producing instability to the resistive interchange mode.

VI. SUMMARY AND DISCUSSION

The nonlinear 3D MHD calculation presented in Sec. IV produced qualitatively similar results as the experimental diagnostic measurements and the equilibrium reconstructions shown in Figs. 1 and 2. The rearrangement of the q and pressure profiles in these non-monotonic q discharges were *not* due to double tearing modes, as often has been speculated.^{15,16,19,20,26,32,33} Rather, it was likely due to nearly ideal MHD modes, as shown in Fig. 5.

The unstable modes with $n \geq 3$ as shown in Fig. 3 are ideal infernal modes, similar to those found for monotonic q -profile discharges with $q_0 > 1$.^{6,7} These modes have their resonance, the surface with q value that satisfies $m - nq = 0$, very close to the minimum in q where the magnetic shear is low. As seen in the figure, these modes are all localized in a narrow band between the two $q = 2$ surfaces. Nonlinearly, these modes will tend to reduce the pressure gradient where they are localized, as seen in Fig. 6. Even though they are basically ideal MHD pressure-driven modes, they can also break magnetic surfaces in their vicinity, even in the limit of vanishingly small resistivity.³⁸

It is very likely that these higher- n modes were responsible for the relatively small decrease in the pressure profile shown in the experimental Fig. 1 between 247 and 267 ms. In the monotonic shear cases, we have examined previously^{6,7} these modes could also destroy the interior magnetic surfaces, leading to temperature flattening. In the present, reversed shear case, the magnetic shear is low only near q_{min} and so the interior surfaces are not as susceptible to breakup.

To nonlinearly change the q and pressure profiles in these equilibria requires a mode with a substantial $m = 1$ component. This is accomplished by the predominantly $n = 1$ harmonic that peaks in Fig. 5 at about $t = 1000 \tau_A$ after the start of the simulation. We see from the first frame of Fig. 3 that it is a pressure driven non-resonant (1, 1) mode that is likely responsible for the large change in the central q and pressure values. We speculate that this mode could also be responsible for the internal reconnection events (IREs) observed in MAST-U discharges with rapid current ramp-up rates.³⁹

In comparing the computational results from Fig. 5 with the experimental MHD signals from Fig. 2, it is clear that the agreement is not exact. The upper graph in Fig. 2 shows a $n = 1$ mode with a large amplitude millisecond blip at about $t = 270$ ms. This has a very rapid onset and decay, and we believe it is the (1, 1) mode calculated in Fig. 5. The experimental $n = 1$ mode in Fig. 2 then starts slowly growing again over the next 20 ms. We speculate that this is a NTM that grows from the perturbation but eventually stabilizes as the pressure decreases sufficiently. This NTM does not occur in the nonlinear simulation as the required neoclassical physics equations are not being solved. Also, the close fitting computational boundary used here tends to stabilize these modes.

The (1, 1) event in the simulation occurs at an earlier time (247+ms) than in the experiment (270 ms). We think that the onset of this mode is sensitive to the value of q_{min} and the details of the pressure profile and our equilibrium reconstruction have error bars that are difficult to quantify so that we may not be able to predict the exact time of the (1, 1) mode onset. Also, as mentioned previously, kinetic effects and sheared toroidal rotation, not included in our nonlinear simulation, may play a role in determining the exact onset time. However, it

is clear that both in the simulation and in the experiment, there is a MHD event that drastically lowers the value of q_0 and the central pressure, and that after this event, the discharge is stable to MHD modes, albeit at a lower value of β .

Finally, we comment on the implications of the $q_0 > 1$ instabilities found here and in previous studies^{6,7} for the next generation of STs, which will presumably be of larger size with stronger magnetic fields. These instabilities can, in principle, be avoided by lengthening the current ramp-up time and avoiding early auxiliary heating. Or, it may be deemed beneficial to “grow” the plasma during the current ramp-up to quicken the current penetration by layering, as has been proposed for ITER.⁴⁰

ACKNOWLEDGMENTS

This work was supported by the U.S. DoE under Award No. DE-AC02-09CH11466 and the SciDAC Center for Tokamak Transient Simulations (CTTS). The calculations were performed on the Perlmutter supercomputer at the National Energy Research Supercomputer Center (NERSC). The authors acknowledge essential software support from J. Chen and the SCOREC team at RPI.

AUTHOR DECLARATIONS

Conflict of Interest

The authors have no conflicts to disclose.

Author Contributions

S. C. Jardin: Conceptualization (equal); Methodology (equal); Software (equal); Writing – original draft (equal). **S. Munaretto:** Conceptualization (equal); Data curation (equal); Writing – review & editing (equal). **N. M. Ferraro:** Software (equal); Validation (equal); Writing – review & editing (equal). **S. M. Kaye:** Funding acquisition (equal); Supervision (equal); Writing – review & editing (equal). **A. Kleiner:** Data curation (equal); Writing – review & editing (equal). **B. C. Lyons:** Software (equal); Validation (equal).

DATA AVAILABILITY

The data that support the findings of this study are available from the corresponding author upon reasonable request.

APPENDIX A: STABILITY OF MODEL EQUILIBRIUM

Here, we describe the stability of model equilibrium with circular cross sections, both in toroidal and cylindrical (or slab) geometry. Consider a toroidal equilibrium with major radius $R = 3.2$ m, minor radius $a = 1.0$ m, and toroidal field on axis $B_0 = 1$ T. We take the pressure and safety factor profiles to be the following functions of the normalized poloidal flux, ψ :¹⁵

$$p(\psi) = p_0 (1.0 - \psi^{\beta_p})^{\alpha_p}, \tag{A1}$$

$$q(\psi) = q_0 \times \left[1 + \left(\frac{\psi}{r_0^2} \right)^\lambda \right]^{\frac{1}{\lambda}} \times \left[1 + A \exp\left(\frac{-\psi}{\delta^2} \right) \right] / (1 + A). \tag{A2}$$

Here, we used $\beta_p = 1.0$, $\alpha_p = 2.0$, $q_0 = 4.5$, $r_0 = 0.612$, $\lambda = 6.48$, $A = 1.64$, and $\delta = 0.23$. These profiles are shown in Fig. 10.

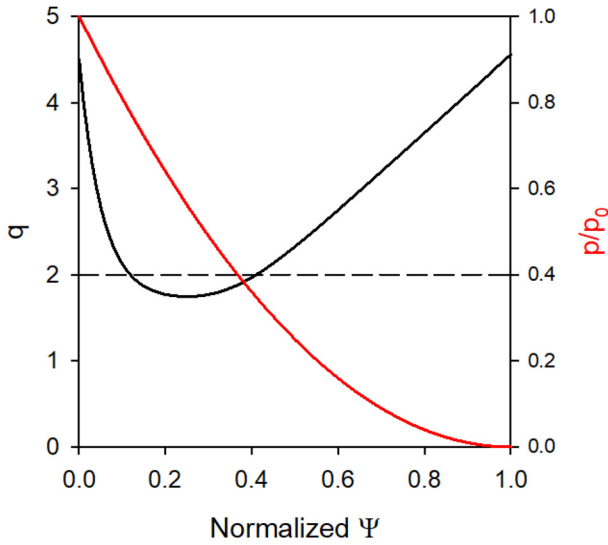


FIG. 10. Profiles for the q and pressure as defined in Eqs. (A1) and (A2).

At zero pressure, $p_0 = 0$, both the toroidal and cylindrical equilibria are unstable to both $n=1$ and $n=2$ double tearing modes. In M3D-C¹, the fluid velocity is represented as $V = R^2 \nabla U \times \nabla \phi + \omega R^2 \nabla \phi + R^{-2} \nabla_{\perp} \chi$. Here, R is the major radius in the torus and a constant in the cylinder. Similarly, ϕ is the toroidal angle in the torus but the symmetry direction in the cylinder. The operator ∇_{\perp} is the gradient in the (R, Z) plane (orthogonal to $\nabla \phi$).

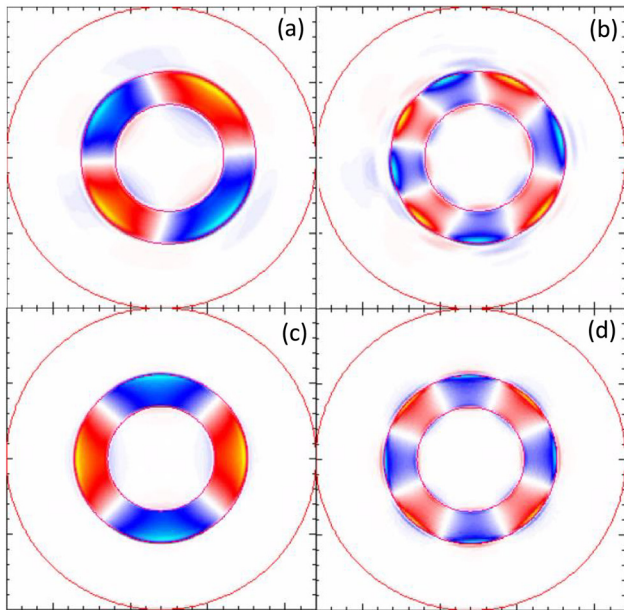


FIG. 11. Velocity stream function, Φ , for (a) the $n=1$ mode in a torus, (b) the $n=2$ mode in a torus, (c) the $n=1$ mode in a cylinder, and (d) the $n=2$ mode in a cylinder. The lines next to the non-zero areas are the contours of $q=2$.

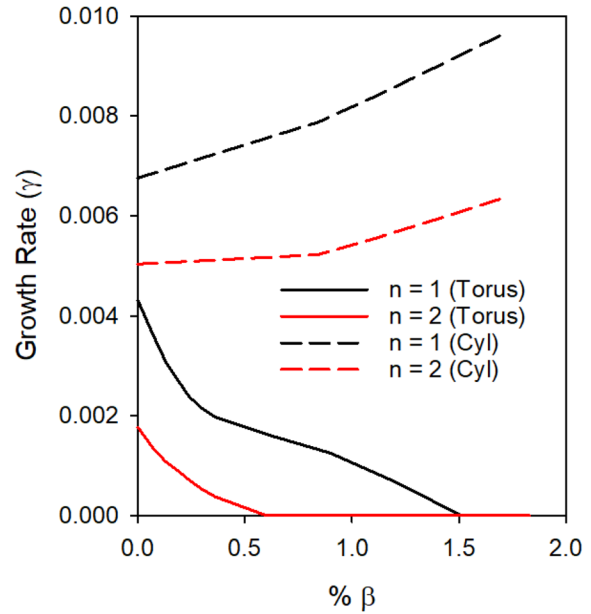


FIG. 12. In the torus, the growth rates for both the $n=1$ and $n=2$ double tearing modes decrease with β , eventually stabilizing. In contrast, in the cylinder, the growth rates for both modes increase with β .

The eigenfunctions for the velocity stream function, U , are shown in Fig. 11 for a calculation with a dimensionless resistivity of $\eta = 1. \times 10^{-6}$.

As we increase the pressure, the growth rates for the $n=1$ and $n=2$ modes in the torus first decrease and then stabilize. In the cylindrical geometry, just the opposite occurs, as the growth rates increase with β . These dependencies are shown in Fig. 12. These linear calculations used a uniform resistivity with a dimensionless value of $\eta = 1. \times 10^{-6}$ as was used in the calculation shown in Fig. 11. Note that the strong stabilizing effect of β in toroidal geometry is consistent with what was found in Ref. 12.

To determine the scaling of the linear growth rates with resistivity, we repeated the zero- β calculation shown in Fig. 12 with two other values of resistivity: $\eta = 0.5 \times 10^{-6}$ and $\eta = 2.0 \times 10^{-6}$. The results are shown in Fig. 13. The dashed lines connecting the $n=1$ results in the cylinder and the torus are what was predicted in Ref. 41 for the $n=1$ double tearing mode in a cylinder using reduced MHD.

Note that the results presented in this section are not meant to be general and apply only to the geometry and profiles used here. However, they do confirm that the stability results of a reversed shear configuration can be very different in cylindrical and toroidal geometry, as was observed in Ref. 12.

APPENDIX B: TRANSPORT COEFFICIENTS IN NONLINEAR CALCULATION

In Table II, we list the numerical values of the normalized transport coefficients appearing in Eqs. (1)–(6) that were used in the nonlinear calculation presented in Sec. IV. The resistivity used

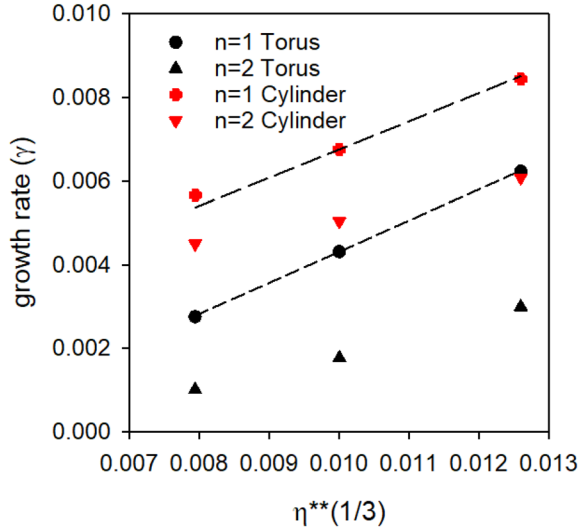


FIG. 13. Growth rates of the $n = 1$ and $n = 2$ modes for the toroidal and cylindrical geometries shown in Fig. 11 as a function of resistivity. Dashed lines show $\eta^{1/3}$ scaling for the $n = 1$ modes.

TABLE II. Transport coefficients for the nonlinear calculation of Sec. IV.

Variable	M3D-C ¹	$t < 900 \tau_A$	$t \geq 900 \tau_A$
ν	AMU	1×10^{-5}	2×10^{-5}
\mathbf{D}	DENM	1×10^{-6}	1×10^{-5}
κ	KAPPAT	1×10^{-6}	1×10^{-6}
$\kappa_{ }$	KAPPAR	1.0	1.0
λ_H	HYPER	1×10^{-9}	1×10^{-9}
f_{η}	ETA FAC	1.0	2.0

was the Spitzer resistivity³⁵ multiplied by a uniform factor, f_{η} , so that $\eta = f_{\eta} \times \eta_{\text{Spitzer}}(T_e)$. In the code's dimensionless units, the initial value of the resistivity at the magnetic axis was $\eta = 4 \times 10^{-9}$. Note that some of the values were changed partway through the calculation to overcome numerical stability issues.

As one of our convergence tests, the nonlinear calculation was repeated with half the value for λ_H . The result for the q -profile at the final time was very similar to that presented in Fig. 7.

APPENDIX C: EXPRESSION FOR D_R

For an axisymmetric configuration, the M3D-C¹ representation for the magnetic field reduces to

$$\mathbf{B} = \nabla \phi \times \nabla \psi + F(\psi) \nabla \phi. \quad (\text{C1})$$

In terms of these variables, the plasma pressure p and the volume enclosed by a flux surface with label ψ , $V(\psi)$, the resistive interchange parameter D_R can be computed as follows:³¹

$$E = -\frac{p'V'}{q'^2(2\pi)^2} \left\langle \frac{B^2}{|\nabla\psi|^2} \right\rangle \left[\frac{Fq'}{\langle B^2 \rangle} + \frac{V''}{(2\pi)^2} \right], \quad (\text{C2})$$

$$F = \left(\frac{p'V'}{(2\pi)^2 q'} \right)^2 \left[F^2 \left(\left\langle \frac{B^2}{|\nabla\psi|^2} \right\rangle \left\langle \frac{1}{B^2 |\nabla\psi|^2} \right\rangle - \left\langle \frac{1}{|\nabla\psi|^2} \right\rangle^2 \right) + \left\langle \frac{B^2}{|\nabla\psi|^2} \right\rangle \left\langle \frac{1}{B^2} \right\rangle \right], \quad (\text{C3})$$

$$H = \frac{-Fp'V'}{(2\pi)^2 q'} \left(\left\langle \frac{1}{|\nabla\psi|^2} \right\rangle - \left\langle \frac{B^2}{|\nabla\psi|^2} \right\rangle \left\langle \frac{1}{B^2} \right\rangle \right), \quad (\text{C4})$$

$$D_R = E + F + H^2. \quad (\text{C5})$$

Here, $\langle a \rangle$ is the standard flux surface average operator that makes $\mathbf{B} \cdot \nabla a$ vanish. The plasma is locally unstable to resistive interchange modes if $D_R > 0$.

REFERENCES

- M. Ono, S. M. Kaye, Y.-K. M. Peng, G. Barnes, W. Blanchard, M. D. Carter, J. Chrzanowski, L. Dudek, R. Ewig, D. Gates *et al.*, "Exploration of spherical torus physics in the NSTX device," *Nucl. Fusion* **40**, 557 (2000).
- H. Meyer, R. J. Akers, F. Alladio, L. C. Appel, K. B. Axon, N. B. Ayed, P. Boerner, R. J. Buttery, P. G. Carolan, D. Ciric, C. D. Challis *et al.*, "Overview of physics results from MAST," *Nucl. Fusion* **49**, 104017 (2009).
- J. E. Menard, S. Gerhardt, M. Bell, J. Bialek, A. Brooks, J. Canik, J. Chrzanowski, M. Denault, L. Dudek, D. A. Gates *et al.*, "Overview of the physics and engineering design of NSTX upgrade," *Nucl. Fusion* **52**, 083015 (2012).
- J. Milnes, N. B. Ayed, F. Dhalla, G. Fishpool, J. Hill, I. Katramados, R. Martin, G. Naylor, T. O'Gorman, and R. Scannell, "MAST upgrade-construction status," *Fusion Eng. Des.* **96**, 42 (2015).
- G. S. Kurskiev, N. N. Bakharev, V. V. Bulanin, F. V. Chernyshev, V. K. Gusev, N. A. Khromov, E. O. Kiselev, V. B. Minnaev, I. V. Miroshnikov, E. E. Mukhin *et al.*, "Thermal energy confinement at the globus-M spherical tokamak," *Nucl. Fusion* **59**, 066032 (2019).
- S. C. Jardin, N. M. Ferraro, W. Guttenfelder, S. M. Kaye, and S. Munaretto, "Ideal MHD limited electron temperature in spherical tokamaks," *Phys. Rev. Lett.* **128**, 245001 (2022).
- S. C. Jardin, N. M. Ferraro, W. Guttenfelder, S. M. Kaye, and S. Munaretto, "Ideal MHD induced temperature flattening in spherical tokamaks," *Phys. Plasmas* **30**, 042507 (2023).
- S. Munaretto, N. M. Ferraro, and E. D. Fredrickson, "On the frequency bifurcations of the MHD startup modes in NSTX," *Phys. Plasmas* **30**, 062502 (2023).
- H. Y. Yuh, F. M. Levinton, R. E. Bell, J. C. Hosea, S. M. Kaye, B. P. LeBlanc, E. Mazzucaro, J. L. Peterson, D. R. Smith, J. Candy *et al.*, "Internal transport barriers in NSTX," *Phys. Plasmas* **16**, 056120 (2009).
- J. E. Menard, R. E. Bell, D. A. Gates, S. M. Kaye, B. LeBlanc, F. M. Levinton, S. S. Medley, S. A. Sabbagh, K. Tritz, and H. Yuh, "Observation of instability-induced current redistribution in a spherical-torus plasma," *Phys. Rev. Lett.* **97**, 095002 (2006).
- H. Y. Yuh, S. M. Kaye, F. M. Levinton, E. Mazzucaro, D. R. Mikkelsen, D. R. Smith, R. E. Bell, J. C. Hosea, B. P. LeBlanc, J. L. Peterson *et al.*, "Suppression of electron temperature gradient turbulence via negative magnetic shear in NSTX," *Phys. Rev. Lett.* **106**, 055003 (2011).
- J. N. Leboeuf, V. E. Lynch, and B. A. Carreras, "Linear and nonlinear resistive magnetohydrodynamic stability of tokamak discharges with negative central shear," *Phys. Plasmas* **8**, 3358–3366 (2001).
- Z. Chang, W. Park, E. D. Fredrickson, S. H. Batha, M. G. Bell, R. Bell, R. V. Budny, C. E. Bush, A. Janos, F. M. Levinton *et al.*, *Phys. Rev. Lett.* **77**, 3553–3556 (1996).
- W. Zhang, Z. Ma, J. Zhu, and W. W. Zhang, "Core-crash sawtooth associated with $m/n = 2/1$ double tearing modes in tokamaks," *Plasma. Phys. Controlled Fusion* **61**, 075002 (2019).
- W. Zhang, X. Lin, Z. W. Ma, X. Q. Lu, and H. W. Zhang, "The off-axis pressure crash associated with the nonlinear evolution of the $m/n = 2/1$ double tearing mode," *Phys. Plasmas* **27**, 122509 (2020).

- ¹⁶P. Maget, G. Huysmans, X. Garbet, M. Ottaviani, H. Lutjens, and J. F. Luciani, "Nonlinear MHD simulation of the tore supra hollow current profiles discharge," *Phys. Plasma* **14**, 052509 (2007).
- ¹⁷P. Maget, H. Lutjens, J. F. Luciani, X. Garbet, O. Fevrier, and J. L. Segui, "Bi-fluid and neoclassical effect of a double-tearing mode in tore supra," *Phys Plasmas* **21**, 062504 (2014).
- ¹⁸P. Maget, H. Lutjens, R. Coelho, B. Alper, M. Brix, P. Buratt, R. J. Buttery, E. DelaLuna, N. Hawkes, G. Huysmans, I. Jenkins, C. D. Challis, C. Giroud, X. Litaudon, J. Mailloux, and M. Ottaviani, "Modelling of (2,1) NTM threshold in JET advanced scenarios," *Nucl. Fusion* **50**, 045004 (2010).
- ¹⁹E. Nardon, V. Bandaru, M. Hoelzl, F. J. Artola, and P. Maget, "Non-linear dynamics of the double tearing mode," *Phys. Plasmas* **30**, 092502 (2023).
- ²⁰A. Bierwage, M. Toma, and K. Shinohara, "MHD and resonant instabilities in JT-60SA during current ramp-up with off-axis N-NB injection," *Plasma Phys. Controlled Fusion* **59**, 125008 (2017).
- ²¹Y. Ishii, M. Azumi, and Y. Kishimoto, "Structure-driven nonlinear instability of double tearing mode and the abrupt growth after long-time-scale evolution," *Phys. Rev. Lett.* **89**, 205002 (2002).
- ²²M. Janvier, U. Kishimoto, and J. Q. Li, "Structure-driven nonlinear instability as the origin of the explosive reconnection dynamics in resistive double tearing modes," *Phys. Rev. Lett.* **107**, 195001 (2011).
- ²³H. Wang, Z.-X. Wang, T. Liu, and X. L. Zhu, "Effects of plasma boundary shape on explosive bursts triggered by tearing mode in toroidal tokamak plasmas with reversed magnetic shear," *Chin. Phys. Lett.* **40**, 075201 (2023).
- ²⁴W. Zhang, Z. Ma, H. Zhang, and X. Wang, "Sawtooth-like oscillations and steady states caused by the $m/2=2/1$ double tearing mode," *Plasma Sci. Technol.* **24**, 035104 (2022).
- ²⁵Q. Yu and S. Gunter, "Fast magnetic reconnection and driven plasma rotation in reversed central magnetic shear configuration," *Nucl. Fusion* **62**, 126056 (2022).
- ²⁶X. Q. Lu, W. Guo, Z. W. Ma, and H. W. Zhang, "Effects of resistivity and viscosity on dynamic evolution and radial position change of $m/n=3/1$ double tearing mode," *Nucl. Fusion* **63**, 066022 (2023).
- ²⁷J. Manickam, N. Pomphrey, and A. Todd, "Ideal MHD stability properties of pressure driven modes in low shear tokamaks," *Nucl. Fusion* **27**, 1461 (1987).
- ²⁸M. N. Rosenbluth and C. L. Longmire, "Stability of plasmas confined by magnetic fields," *Ann. Phys.* **1**, 120–140 (1957).
- ²⁹J. L. Johnson and J. M. Greene, "Resistive interchange and the negative V'' criterion," *Plasma Phys.* **9**, 611–629 (1967).
- ³⁰A. H. Glasser, J. M. Greene, and J. L. Johnson, "Resistive instabilities in general toroidal plasma configurations," *Phys. Fluids* **18**, 875 (1975).
- ³¹A. H. Glasser, J. M. Greene, and J. L. Johnson, "Resistive instabilities in a tokamak," *Phys. Fluids* **19**, 567–574 (1976).
- ³²M. S. Chu, J. M. Greene, L. L. Lao, R. L. Miller, A. Bondeson, O. Sauter, B. W. Rice, E. J. Strait, T. S. Taylor, and A. D. Turnbull, "Resistive interchange modes in negative central shear tokamaks with peaked pressure profiles," *Phys. Rev. Lett.* **77**, 2710–2713 (1996).
- ³³T. C. Hender, P. Hennequin, B. Alper, T. Hellsten, D. F. Howell, G. T. Huysmans, E. Joffrin, P. Maget, J. Manickam, M. F. Nave *et al.*, "MHD stability with strong reversed magnetic shear in JET," *Plasma Phys. Control Fusion* **44**, 1143–1154 (2002).
- ³⁴S. C. Jardin, N. Ferraro, J. Breslau, and J. Chen, "Multiple timescale calculations of sawteeth and other global macroscopic dynamics of tokamak plasmas," *Comput. Sci. Discovery* **5**, 014002 (2012).
- ³⁵J. D. Huba, *NRL Plasma Formulary, Revised* (IOP Publishing, 2013).
- ³⁶L. D. Landau and E. M. Lifschitz, in *Fluid Mechanics*, 1st ed. (Pergamon Press, 1959), Vol. 6.
- ³⁷S. Jardin, "A triangular finite element with first-derivative continuity applied to fusion MHD applications," *J. Comput. Phys.* **200**, 133–152 (2004).
- ³⁸A. H. Boozer, "The rapid destruction of toroidal magnetic surfaces," *Phys. Plasmas* **29**, 022301 (2022).
- ³⁹J. W. Berkery, S. A. Sabbagh, L. Kogan, S. Gibson, D. Ryan, V. Zamkovska, J. Butt, J. Harrison, S. Henderson, and MAST-U Team, "Operational space and performance limiting events in the first physics campaign of MAST-U," *Plasma Phys. Controlled Fusion* **65**, 045001 (2023).
- ⁴⁰S. C. Jardin, C. E. Kessel, and N. Pomphrey, "Poloidal flux linkage requirements for the International Thermonuclear Experimental Reactor," *Nucl. Fusion* **34**, 1145 (1994).
- ⁴¹P. L. Pritchett, Y. C. Lee, and J. F. Drake, "Linear analysis of the double tearing mode," *Phys. Fluids* **23**, 1368–1374 (1980).